ISSN 1995-0780, Nanotechnologies in Russia, 2013, Vol. 8, Nos. 7–8, pp. 466–481. © Pleiades Publishing, Ltd., 2013.
Original Russian Text © S.Yu. Sokovnin, V.G. Il'ves, A.I. Surdo, I.I. Mil'man, M.I. Vlasov, 2013, published in Rossiiskie Nanotekhnologii, 2013, Vol. 8, Nos. 7–8.

Effect of Iron Doping on the Properties of Nanopowders and Coatings on the Basis of Al_2O_3 Produced by Pulsed Electron Beam Evaporation

S. Yu. Sokovnin[a, b], V. G. Il'ves[a], A. I. Surdo[b, c], I. I. Mil'man[b], and M. I. Vlasov[c]

[a] *Institute of Electrophysics, Ural Branch, Russian Academy of Sciences, Yekaterinburg, 620016 Russia*
[b] *Ural Federal University, Yekaterinburg, 620002 Russia*
[c] *Institute of Industrial Ecology, Ural Branch, Russian Academy of Sciences, Yekaterinburg, 620219 Russia*
e-mail: sokovnin@iep.uran.ru

Received October 4, 2012; in final form, April 11, 2013

Abstract—Multiphase nanopowders (NPs) and amorphous/amorphous-nanocrystalline coatings (A-NC) have been prepared by the evaporation of ceramic targets of Al_2O_3-Fe_2O_3 (0.1, 3, 5 Fe_2O_3 mass %) by a pulsed electron beam in vacuum. The specific surface area of NP Al_2O_3-Fe_2O_3 reached 277 m^2/g. The α and γ phases Al_2O_3 and other nonidentified phases have been found in the composition of NP Al_2O_3-Fe_2O_3. All coatings contained an insignificant fraction of the crystalline γ phase. No secondary phases on the basis of iron have been revealed. According to transmission electron microscopy, the fine fraction of NP Al_2O_3-Fe_2O_3 consists of amorphous nanoparticles of an irregular and quasispherical shape no more than 10 nm in size which form agglomerates reaching 1.5 μm. A large fraction of NPs consists of crystal spherical nanoparticles with preferential sizes of about 10–20 nm. All NP Al_2O_3-Fe_2O_3 showed ferromagnetic behavior at room temperature. The maximum magnetic response has been established in NPs with a minimum iron content (1.1 mass %). The pulsed cathode luminescence spectra of coatings and NP Al_2O_3-Fe_2O_3 have been presented by a wide band in the wavelength range of 300–900 nm regardless of their phase composition. Phase transformations into NP AL_2O_3-1.1% Fe and coatings from undoped Al_2O_3 heated to 1400°C occur according to the following scheme: amorphous phase $\rightarrow \gamma \rightarrow \delta \rightarrow \theta \rightarrow \alpha$, regardless of their initial phase composition. The threshold of thermal stability of the γ phase in NPs and the coating of undoped Al_2O_3 does not exceed 830°C. For the first time, the increased thermo and optically stimulated luminescent response comparable with the response of the leading TLD-500K thermoluminescent dosimeter has been reached in A-NC coatings of undoped Al_2O_3.

DOI: 10.1134/S1995078013040186

INTRODUCTION

Thin Al_2O_3films are widely used as wear-resistant and diffusion-barrier coatings. The solid and stable α phase of Al_2O_3 is used more often in high-temperature applications. The presence of intermediary metastable phases (no less than 24 polymorphous phases of Al_2O_3 are known [1]) complicates the growth of the α phase of Al_2O_3, particularly at low temperatures. Studies of low-temperature growth directed at the formation of the α phase are intensively developed. Let us note the works where the α-Al_2O_3 films were obtained at 760°C by reactive magnetron sputtering [2], at 580°C using plasma-enhanced chemical vapor deposition [3], at 280–560°C by the nonreactive radio-frequency magnetron sputtering of the target to the nucleation layers of Cr_2O_3 oxide [4, 5], and at 500°C using a template of Cr_2O_3 by reactive magnetron sputtering [6].

It is known that there is a large number of works on the preparation of amorphous and amorphous-nanocrystalline (A-NC) films [7, 8], coatings [9, 10], and submicron- and NPs (NPs) [11, 12] on the basis of Al_2O_3 using different high-temperature methods: pulsed laser evaporation [13, 14], continuous and pulsed electron evaporation [15, 16], different modifications of magnetron sputtering [9, 10], plasma-chemical technologies [17,18], detonation synthesis [19, 20], etc.

The results of these studies indicate that the ways of the formation and phase transformation of different materials on the basis of Al_2O_3 during further annealing are characterized by exclusive variety and depend on many factors: the method used and the conditions of synthesis (deposition time, crystallization rate, and pressure and composition of the gaseous phase), temperature and crystallographic orientation of the substrate material [21, 22], etc.

The amorphous phase, which usually transforms into the γ phase of Al_2O_3 during further annealing, is

most often formed during the deposition of thin films on relatively cold substrates (25–250°C [23–25]) by means of electron evaporation. In turn, depending on the method of the preparation, the γ phase may remain thermally stable up to very high temperatures on the order of 1000–1100°C [7].

On the one hand, the introduction of different dopants into Al_2O_3 makes it possible to control the crystallization temperature of the amorphous phase [25]; on the other hand, iron doping may lead to unexpected phase transformations during further annealing, e.g., amorphous phase → α phase Al_2O_3 [17]. In [17], amorphous NP Al_2O_3 doped with 0.1 mole Fe was obtained using the plasma-chemical method, which was transformed into the stable α phase of Al_2O_3 at a record low temperature of 143°C after annealing in air. The typical transformation of the amorphous phase into the γ phase of Al_2O_3 was observed with the increase in the iron concentration of up to 0.6 mole.

The plasma-chemical method [17] and evaporation by means of pulsed electron beam (PEB) make it possible to produce nanoparticles (NPs) of a similar size (2–8 nm); therefore, it was interesting to reproduce the achievements of [17] by means of the electron evaporation and to simultaneously study the effect of iron on the different characteristics of the Al_2O_3-Fe_2O_3 samples at a low doping level, which is studied insufficiently.

In particular, the α phase of Al_2O_3 is widely applied in dosimetry [26]. However, the production of commercial thermoluminescent dosimeters (TLDs) [26] of anion-defective corundum is based on the use of the unprofitable and long-term high-temperature growth of an Al_2O_3 rod in the reduction medium with the subsequent mechanical processing of the rod with considerable screening.

The application of thin films (coatings) or NPs of Al_2O_3 in a working medium of a TLD may become a good alternative to the above method of producing radiation detectors. In this case, parameters such as hardness, wear resistance, etc., become of less importance, and the transparency of oxide coatings and films makes it possible to apply them in dosimetry using optically stimulated luminescence.

The trend of TLD developers of using the thermostable α phase of Al_2O_3 as radiation detectors and the limited number of studies where amorphous or metastable phase Al_2O_3, which often has rather high thermal stability up to 1000–1100°C [27], was used as the working medium of the dosimeter indicate the drawbacks in the studies of this field.

In addition, the use of electron-beam technology for producing NPs and thin films or coatings makes it possible to transfer the technology of producing radiation detectors to the industrial level.

This work was aimed at producing A-NC coatings and NPs on the basis of pure and iron-doped oxide Al_2O_3 by means of the pulsed electron evaporation in vacuum and studying their structural, magnetic, luminescent, and dosimetric characteristics; thermal stability; and sequences of phase transformations during annealing in air up to a temperature of 1400°C.

EXPERIMENTAL METHODOLOGY

Coatings and NPs were produced by the evaporation of ceramic targets in vacuum (the residual pressure is 4 PA) using a pulsed electron beam on a NANOBIM-2 setup [28]. The target was round disks with a diameter of 60 mm and height reaching 20 mm obtained by sintering pressings made on a hand press of α-Al_2O_3 NP (IAM, United Sates) with additives of a micron powder (1, 3 and 5 wt %) of α phase Fe_2O_3 (analytically pure grade, GOST 4173-77) in air at a temperature of 1000°C for 1 h.

The energy of electrons was 40 keV, the energy of the electron beam pulse was 1.8 J, the pulse duration was 100 μs, and the pulse frequency was 100–200 Hz. Coatings and NPs were produced under the same conditions with different deposition times (5–10 min for coatings; 40–60 min for NPs) and the target-substrate distance (5 cm for coatings; ≈10–15 cm for NP). Coatings were deposited on the cover glasses (5 cm × 2.4 cm) with a thickness of 0.13–0.18 mm; NPs were deposited on the substrates of window glass with a thickness of 4 mm and a large area placed around the target.

The following diagnostics were used for studying the properties of NPs and coatings. The X-ray analysis (XRD) was performed on XRD 7000 Shimadzu (Japan) and X'PERT PRO (The Netherlands) diffractometers. The specific surface of powders (S_{sp}) was determined by the BET method on a Micromeritics TriStar 3000 setup. The heating/cooling thermograms and mass spectra were recorded by means of differential scanning calorimetry (DSC) and thermogravimetry (TG) methods on a STA-409-PC Luxx synchronous thermoanalyzer combined with a QMS-403C mass spectrometer (NETZSCH).

The microscopic analysis of NPs was performed on a JEOL JEM 2100 transmission electron microscope. The chemical analysis was performed by the inductive-coupled plasma (ICP) method on an iCAP 6300 Duo spectrometer. The pulsed cathode luminescence (PCL) was studied on a KLAVI-1 setup [29]. The magnetic characteristics were established on a Faraday balance, the sensitivity of the balance was $\sim 10^{-5}$ emu, and the magnetic field range of the measurements reached12 kOe.

The decay curves of the optically stimulated luminescence (OSL) in the continuous stimulation mode, the thermoluminescence (TL) curves, and the spectral composition of TL were studied on a specially designed automated setup [30]. The samples were excited by the β radiation of the $^{90}Sr/^{90}Y$ source (P =

Specific surface, Fe concentration (ICP), and average diameter of nanoparticles in NP Al_2O_3–Fe_2O_3

Sample no.	1	2	3	4
Composition of the target*	Al_2O_3 [16]	Al_2O_3–1%Fe_2O_3	Al_2O_3–3% Fe_2O_3	Al_2O_3–5% Fe_2O_3
S_{sp}, m^2/g	270	160	277	222
x_{Fe} (wt %)	0.06	1.1	2.5	4.1
d_{BET}^{**}	7.4	9.3	5.4	6.7

* The Fe_2O_3 content in the targets is given in wt %.
** The density of the amorphous phase $\rho_{amor} = 3.0$ g/cm^3 [35] and the density of bulk $Al_2O_3 = 4.0$ g/cm^3 were used in the calculation of d_{BET}.

0.5 mGy/s) and X-ray radiation (Rh-anode, U = 30 kV, I = 1–40 μA). TL and OSL signals were registered by FEU-106 and FEU-142 photomultipliers and using an MSD-2 monochromator. The continuous stimulation mode was used for the measurement of the OSL decay curves. The stimulation sources were light-emitting diodes of the blue ($\lambda_{max} = 470$ nm) luminescence of the SDK-S469-5-10 type. A UFS-2 filter was used for separating the stimulating radiation from the OSL signal. TLD-500K detectors on the basis of anion-defective corundum (α-$Al_2O_{3-\delta}$) single crystals with average sensitivities were used for comparative studies of the luminescent and dosimetric properties.

EXPERIMENTAL RESULTS AND DISCUSSION

NPs and A-NC coatings of Al_2O_3-Fe_2O_3 with thicknesses of 20–40 μm on substrates of heterogeneous materials with weak adhesion to the substrate material were prepared in the experiments.

The table shows the parameters of the specific surface (S_{sp}) of NP Al_2O_3-Fe_2O_3, the Fe content in NP (x_{Fe}), and the average size of the particles d_{BET}.

The considerable deviation of the chemical composition of NPs from the composition of the targets is due to the difference in the partial pressures of iron and aluminum oxides during evaporation at high temperatures. Data in the table show that S_{sp} of NP Al_2O_3-Fe_2O_3 changes nonmonotonically with increasing $x_{Fe.}$ The sharp decrease in S_{sp} at the low doping level ($x_{Fe} = 1.1$ wt %) in comparison with the surface multiphase NPs of pure Al_2O_3 [16] indirectly indicates the formation of solid solutions $(Al_{1-x}Fe_x)_2O_3$ in the polymorphous phases (α, γ, etc.) in the composition of the multiphase powder $x_{Fe} = 1.1\%$. The tendency toward a decrease in the specific surface in the Al_2O_3-Fe_2O_3 system with an increase in the Fe_2O_3 concentration from 0 to 100% (sol-gel method) was traced in [31] and is in agreement in part with our data.

The smooth change of the color of doped powders from white to light yellow with increasing Fe concentration clearly demonstrates the increase in the solubility of iron atoms in the Al_2O_3 lattice. In the limiting case, the multiphase NPs (the relative content of the crystalline phases was FeO-61%, Fe_3O_4-27%, Fe_2O_3-12%) with the amorphous component (≈30% of the volume)) we obtained earlier by the evaporation of the Fe_2O_3 oxide target, had a vividly expressed brown color [32].

The difference in the color of Al_2O_3-Fe_2O_3 coatings with increasing x_{Fe} is less clear because of their small thickness (tens of micrometers).

According to the XRD data, no secondary phases containing Fe were found in the composition of NP Al_2O_3-Fe_2O_3 ($x_{Fe} = 1.1\%$). The absence of secondary phases indicates the implantation of Fe atoms in the Al_2O_3 lattice and the possible formation of solid solutions $(Al_{1-x}Fe_x)_2O_3$ on the basis of its polymorphous phases.

The diffractograms of NP and A-NC coatings on the basis of Al_2O_3-Fe_2O_3 are given in Figs. 1 and 3.

The diffractograms of samples are almost identical. There is a slight difference in the intensity of separate reflexes. Two phases are reliably identified: α and γ phases of Al_2O_3 (cards PDF-2: 01-070-5679 and 00-010-0425, respectively). The peaks are noticeably shifted to the small-angle region in comparison with PDF-2 data. The reflexes of a series of unidentified phases are present in diffractograms (Fig. 1a). The narrow and intense peaks denoted with black stars in Fig. 1a most likely belong to one phase. It was not possible to calculate the unit-cell parameters and half-width of reflexes for γ- and α-Al_2O_3 phases because of the large number of unidentified phases and the considerable overlap of reflexes (Fig. 1b). The width of the reflex of the α phase of Al_2O_3 in sample 3 from the table was correctly estimated from the peak (012), $x_c(2\theta) = 25.289$ degrees, $\omega = 0.166 \pm 0.05$; the average size of the coherent scattering regions (CSR) was 151 nm.

The diffractogram of the sample Al_2O_3-1.1% Fe (Fig. 1b, sample *2*) shows additional reflexes in the angle range of 30–60° (denoted with arrows).

In contrast to the results [17], the multiphase nanocrystalline powders containing α and γ phases of Al_2O_3 and a series of other unidentified phases were obtained in our case during the deposition of NPs on the cold glass substrate. No amorphous phase was found in NPs using XRD.

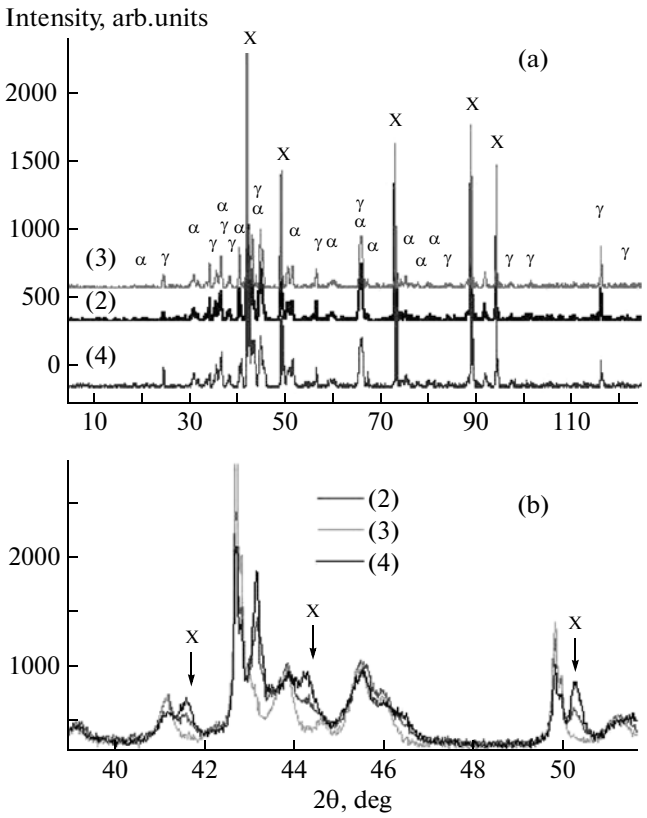

Fig. 1. (a) Diffractograms of NP Al_2O_3-Fe_2O_3 samples (the table, samples 2–4). X denotes the nonidentified phase; (b) enhanced fragment of the NP Al_2O_3-Fe_2O_3 diffractogram in the range of angles $2\theta = 40–50°$. Arrows denote the peaks of the unidentified X phase in sample 2 (the table).

We note that the Fe_2O_3-(1,3,9 wt %) Al_2O_3 samples were studied in [33] and a strong perturbation of the crystal phase Fe_2O_3 was noted in the diffractogram of the sample 91%Fe_2O_3 -9%Al2O3, and a series of unidentified peaks, the presence of which were associated with the formation of $(Al_xFe_{1-x})_2O_3$ solid solutions in the oxide system, were also observed in X-ray spectra. Interestingly, authors [33] noted the domination of the amorphous phase in the sample Fe_2O_3-(9 wt %) Al_2O_3 (Al_2O_3 has a tendency to easier amorphization when compared with Fe_2O_3).

In [31], the presence of phases α-Al_2O_3 and hematite was shown in a series of Al_2O_3-(0–100%) Fe_2O_3 samples by means of XRD. The analysis of Moessbauer spectra also showed the presence of two iron-containing phases.

We note that the formation of α and θ phases in NPs based on pure Al_2O prepared by different high-temperature gas-phase methods (PLD, the electric explosion of wires, evaporation by the continuous electron beam, CVD, and MOCVD) was not observed earlier. A slight fraction of the α phase of Al_2O_3 (30%) was produced only in the multiphase detonation coatings [34].

Thus, our XRD data and those of [31, 33] indicate a rather complicated mechanism of the phase formation of different materials in the Al_2O_3-Fe_2O_3 system regardless of the preparation method and dopant concentration.

The microscopic analysis of NP Al_2O_3-Fe_2O_3 (x_{Fe} = 1.1% Fe) showed (Fig. 2) that the NP consists of fine-crystalline and large-crystalline fractions. The fine fraction (Fig. 2a) is agglomerates up to 1–1.5 μm in size which consist of amorphous NPs of irregular and quasi-spherical shapes with sizes of ~3–10 nm. The separate large NPs of a spherical shape with a diameter of ~20–30 nm in the composition of the fine fraction have a core-shell structure: a crystal core and an amorphous shell with a thickness of ~2–3 nm (Fig. 2b). The large fraction contains mainly crystal NPs of a spherical shape with different diameters of ~10–20 nm (Fig. 3c). The electronograms of NPs of the large frac-

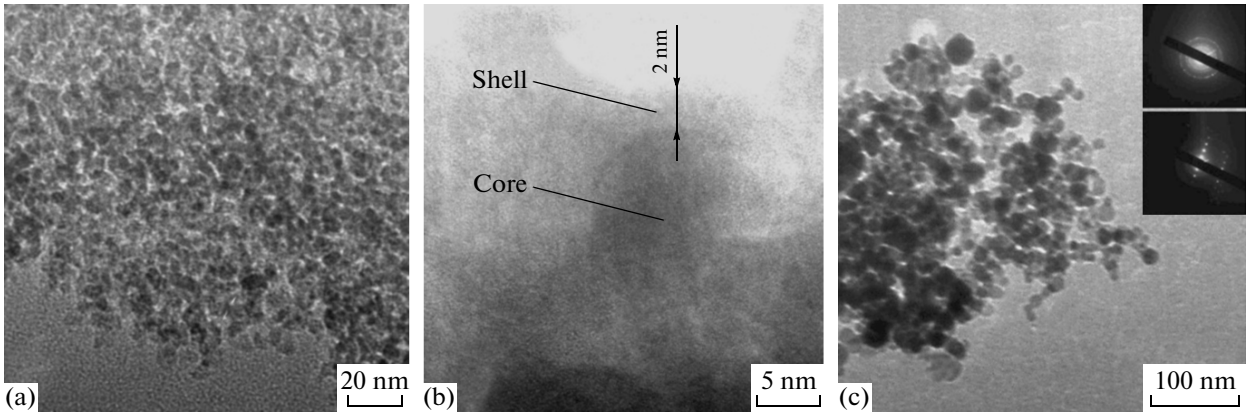

Fig. 2. TEM and TEM HR photos of NP Al_2O_3-1.1%Fe: (a) TEM photo of amorphous NPs of the fine fraction; (b) core-shell NP in the fine fraction; (c) particles of the large-crystalline fraction of NP (inset shows the point and ring reflexes on electronograms of the crystalline NP).

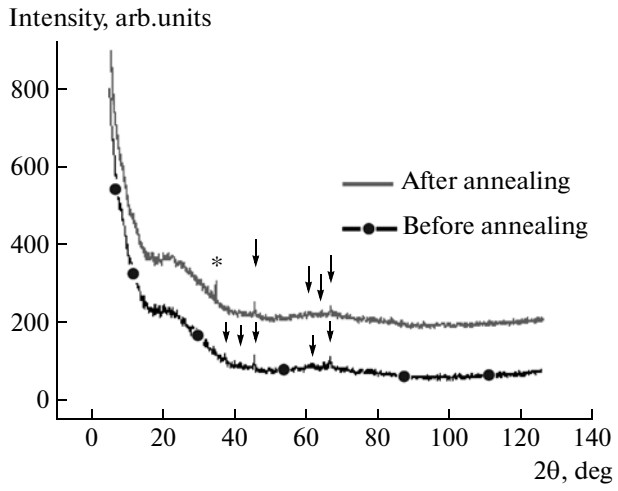

Fig. 3. Diffractograms of the A-NC coatings Al_2O_3-1.1% Fe before and after annealing in air at a temperature of 300°C for 2 h processed with smoothening over 5 points.

tion show normal point and ring reflexes (inset in Fig. 2c).

In contrast to NPs, Al_2O_3-Fe_2O_3 coatings mainly contained an amorphous component. Figure 3 show the diffractograms of Al_2O_3-Fe_2O_3 coatings (1 wt % Fe) deposited in 5 min before and after annealing in air at a temperature of 300°C for 2 h. The diffractogram of the nonannealed coating shows peaks characteristic for the γ-Al_2O_3 phase (PDF-card 00-010-0425). A reflex near $2\theta \approx 34.4°$ appeared after annealing (denoted in Fig. 2 by the symbol *), which is not typical for γ-Al_2O_3. Most likely, the reflex at $2\theta \approx 34.4$ corresponds to the δ-Al_2O_3 phase (card 00-046-1215). However, it is rather complicated to unambiguously interpret the visible changes in the diffractograms of the coating before and after annealing, since the intensity of the reflexes is small.

The conditions of the preparation of NPs and coatings differed in the deposition time and the target-substrate distance.

Thus, it was established that the phase composition of coatings and NPs depended on the NP deposition time. Probably the long-term thermal action (the deposition time of NP was 40–60 min) at the successive layered deposition of NP on the cold substrate induced the crystallization of the amorphous phase in the NP and led to the formation of several crystalline phases.

The effect of the plasma torch from the evaporated target on the change of the phase composition of NPs is of low probability because of the large distance between the target and substrates (10–15 cm). On the contrary, the effect of the thermal action of the plasma torch on coatings is not excluded during the deposition of coatings because of the small target-substrate distance (5 cm).

Coatings of pure Al_2O_3 that we prepared earlier by deposition in vacuum were also either purely amorphous or A-NC with a fine fraction of the γ phase of Al_2O_3 in the amorphous matrix. However, Al_2O_3-Fe coatings always contained a small fraction of the γ phase.

The absence of noticeable growth of the new nanocrystals of the γ phase in the Al_2O_3-1.1% Fe coating (Fig. 3) after annealing at a temperature of 300°C is in agreement with the DSC data of the thermogram of NP Al_2O_3 –1.1% Fe (Fig. 4a). It is seen that the crystallization of the amorphous phase in NPs (exothermal peak) starts from a temperature of about 470°C. If it is assumed that the crystallization of the amorphous phase takes place similarly in the coating and NP, the absence of the growth of the new crystals of the γ phase in the coating (the growth of the new nanocrystals of the γ phase was observed during annealing (300°C) in the coating of pure Al_2O_3 (not given here)) indicates the inhibiting effect of the iron additives on the temperature of the crystallization of the amorphous phase.

Figure 4a shows a thermogram of the synchronous DSC-TG heating of the multiphase NP Al_2O_3-Fe_2O_3 (1.1 wt % Fe). The first two first endothermal peaks (**1**) on the DSC curve are caused by the evaporation of adsorbed water from the NP surface. The exothermal peak in the temperature range of 470–825°C corresponds to the crystallization of the amorphous component of NP leading to the formation of the γ phase of Al_2O_3. Two subsequent exothermal peaks in the temperature intervals of 825–910°C (**2**) and 910–1220°C (**3**), most likely, are due to the subsequent phase transformations $\gamma \rightarrow \delta$ and $\delta \rightarrow \theta$. The exothermal peak (**4**) from the final transformation $\theta \rightarrow \alpha$ is clearly seen in the DSC curve with a temperature of 1220°C. The incomplete transformation of the θ phase of NPs into the stable phase α-Al_2O_3 is indicated by the powerful thermal peak in the cooling curve at a temperature of about 1120°C (Fig. 4b).

It follows from the TG curve (Fig. 4a) that the evaporation of water from NPs ends at a rather low temperature of about 500°C. The nonmonotonic growth of the mass sample upon a further increase in temperature is most likely associated with the annealing of defects (oxygen vacancies), the number of which changes in a complicated manner as a result of the change in the NP structure in the course of the consecutive phase transformations. The continuous growth of the NP mass to a temperature of 1400°C indicates that the defects in the NP are conserved even at a very high temperature. It is known that, at the initial stage of heating γ-phase Al_2O_3, its specific surface increases as a result of the formation of the nanosize pores (2–3 nm) [35]. In particular, it was shown in [36] that the introduction of the tungsten atoms in amorphous Al_2O_3 leads to the growth of the number of

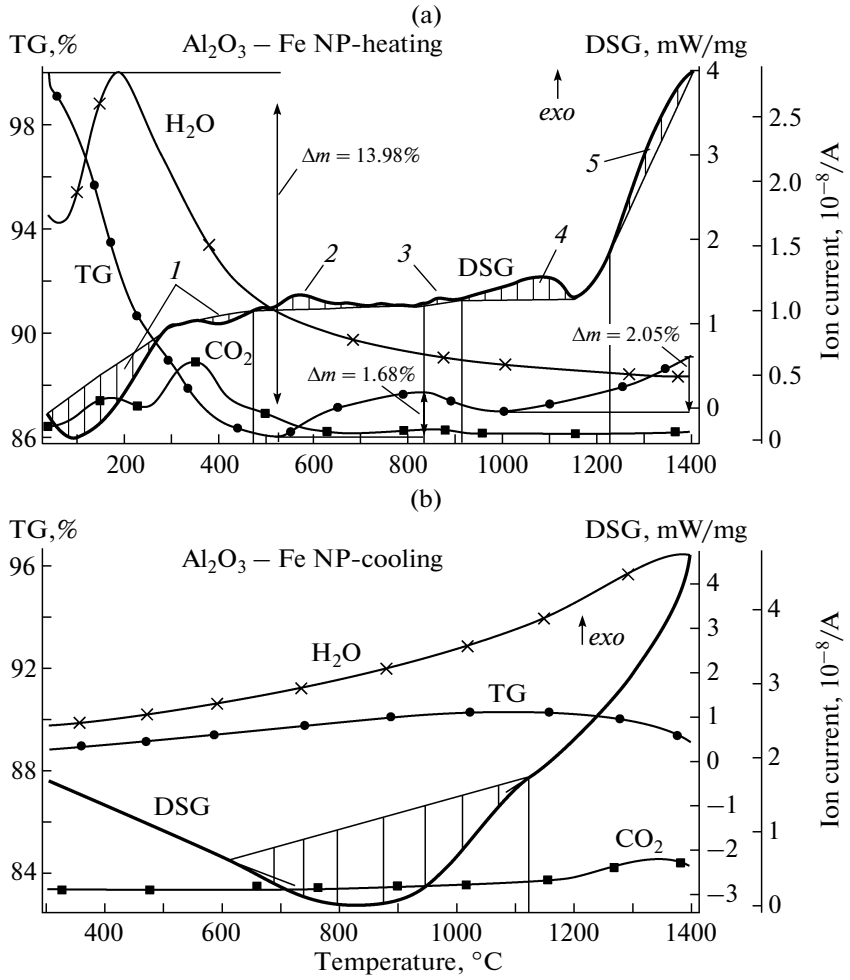

Fig. 4. (a) DSC-TG heating thermograms and mass spectra of H_2O and CO_2 of NP Al_2O_3-Fe_2O_3 (1.1% Fe). (*1*) Evaporation of the adsorbed water, (*2*) crystallization of the amorphous phase in γ-phase Al_2O_3, (*3*) $\gamma \rightarrow \delta$, (*4*) $\delta \rightarrow \theta$, and (*5*) $\theta \rightarrow \alpha$). (b) DSC-TG cooling thermograms and mass spectra of H_2O and CO_2 NP Al_2O_3-1.1% Fe. The heating/cooling rate is 10°C/min.

nanopores in comparison with the number of nanopores in pure Al_2O_3. It is not excluded that a similar effect can be produced by the Fe atoms on the amorphous Al_2O_3-Fe_2O_3 coatings prepared by electron evaporation. The crystallization of the amorphous phase in NP at the initial stage of heating leads to an increase in the concentration and grinding of nanocrystals of the γ phase and, respectively, to an increase in the number of oxygen vacancies, causing a further increase in the sample mass due to annealing vacancies with increasing temperature. The temperature range of the crystallization of the amorphous phase (475–825°C) indicates that the threshold of the thermal stability of the γ phase in NP Al_2O_3-Fe_2O_3 is limited from above by a temperature of 825°C. The sequence of the phase transformations in NP Al_2O_3-Fe_2O_3 occurs according to the scheme amorphous phase $\rightarrow \gamma \rightarrow \delta \rightarrow \theta \rightarrow \alpha$, which is well known from the literature during the crystallization of the melt Al_2O_3 and the stabilization of the α phase from boehmite and amorphous anodized films [21]. We note that, in the literature, the problem about the reversibility of the phase transformations of the metastable phases of Al_2O_3 is treated rather poorly; in particular, the absence of the reversible transformations with decreasing temperature was underlined in [21]. However, the presence of the large thermal effect on the cooling curve of NP Al_2O_3-Fe_2O_3 (Fig. 4b) makes the reliability of this statement doubtful [21]. It was shown is a series of works that the reversible transformation of the stable α phase according to the reaction $\alpha \rightarrow \gamma$ is possible under the action of the compression and shift during vibro loading [37]; high pressure, temperature, and shear strains in the contact points [38]; and during the irradiation of corundum ceramics by fast neutrons [39].

We also observed considerable thermal effects on the DSC cooling curves in multiphase NPs on the basis of pure Al_2O_3 and Al_2O_3-Cu (1.7 wt % Cu) [16] preliminarily heated to a temperature of 1400°C,

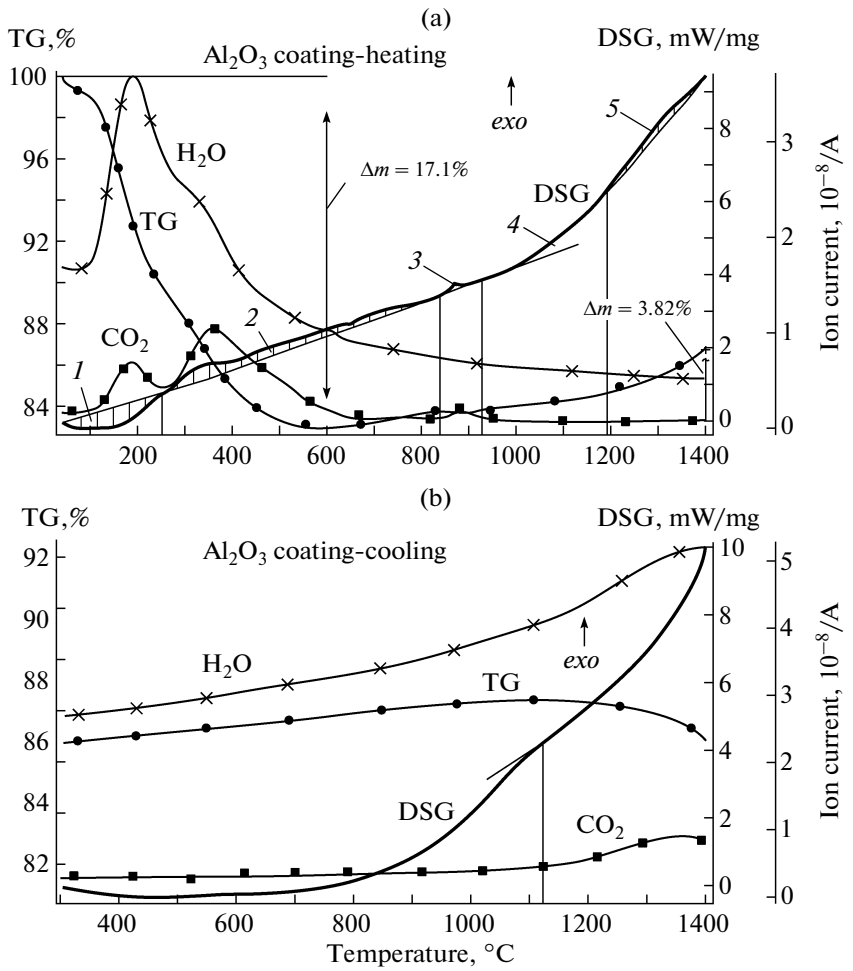

Fig. 5. (a) DSC-TG heating thermograms and mass spectra H_2O and CO_2 amorphous-nanocrystalline coatings Al_2O_3. (*1*) Evaporation of the adsorbed water, (*2*) crystallization of the amorphous phase in the γ phase Al_2O_3, (*3*) $\gamma \rightarrow \delta$, (*4*) $\delta \rightarrow \theta$, and (*5*) $\theta \rightarrow \alpha$). (b) The thermograms cooling DSC-TG and mass spectra of H_2O and CO_2 of amorphous-nanocrystalline coatings Al_2O_3-Fe_2O_3 (1.1% Fe). Heating and cooling speed: 10°C/min.

which indicates the possibility of the reversibility of polymorphous transformations in the metastable phases of Al_2O_3; however, a study of this problem is outside the scope of this work.

To study the phase transformations in the coating of pure Al_2O_3 (according to the XRD data, the amorphous coating contained about 16 wt % of the crystal γ-phase Al_2O_3), we prepared a sample taken from the glass substrate using a titanium foil. The phase transformations in the A-NC coating of pure Al_2O_3 also occur according to the scheme amorphous phase $\rightarrow$ $\gamma \rightarrow \delta \rightarrow \theta \rightarrow \alpha$. First, the adsorbed water is evaporated from the coating (the endothermal peak **1** in Fig. 5a). The crystallization of the amorphous phase starts at much lower temperature (250°C, exothermal peak **2**) than in NP Al_2O_3-1.1% Fe (470°C). This may be caused by the catalytic effect of water vapors on the temperature of the crystallization of the amorphous phase [40]. The temperature of the beginning of the transformation $\gamma \rightarrow \delta$ (830°C, exothermal peak **3**) in the coating almost coincides with the analogous temperature in NP Al_2O_3-1.1% Fe. However, the exothermal peak **4** of the transformation $\delta \rightarrow \theta$ in the coating is expressed much more weakly than in NPs. The transformation $\theta \rightarrow \alpha$ in the coating (exothermal peak **5**) also starts at a much lower temperature (~1080°C) than in NP. Obviously, the iron doping of Al_2O_3 has an inhibiting effect on the temperature of the crystallization of the amorphous phase and the temperature of the phase transformations $\theta \rightarrow \alpha$, but it does not affect the temperature of the polymorphous transformations of other intermediary phases. It is seen in the TG curve that water is evaporated from the coating at a temperature of about 600°C. The further nonmonotonic growth of the mass of the sample analogous to the growth of the mass of the sample in NP Al_2O_3-1.05% Fe is most likely associated with the annealing of defects (oxygen vacancies) that occurs up to a temperature of 1400°C.The presence of the thermal effect on the DSC cooling curve of the coating (Fig. 5b) is also

confirmed by the absence of the final transformation of the coating into the stable α phase of aluminum upon heating to 1400°C and the possibility of the reversible transformation of the metastable phases during cooling.

The search for room temperature ferromagnetism (RTFM) in diluted magnetic semiconductors and oxides is one of the most intriguing fields in modern physics of magnetism [41–43]. In particular, RTFM in undoped Al_2O_3 (so-called d° ferromagnetism [44]) was found in [45, 46]. Earlier, we also established the presence of RTFM in NP Al_2O_3-Cu (Al) [16], ZnO, ZnO-Zn [47], ZnO-Zn-Cu [48], ZnO-Zn-Fe [31, 49], CeO_2, CeO_2-C, CeO_2-Cu [50], and ZnS, ZnS-Al [51].

Physical properties of nanocomposite materials consisting of metal or oxide nanocrystals embedded in the dielectric matrix differ strongly from the physical properties of the corresponding bulk materials. The properties of such materials can be changed not only by the size, shape, and content of the embedded NP, but also by the nature of the matrix and interface between the NP and the matrix. When metal NP is embedded in the oxide matrix, it is rather difficult to avoid the oxidation and agglomeration of particles in the synthesis process of the nanocomposite, which is in part prevented by the low solubility of metal particles in the matrix. On the contrary, the rather high boundary of the solubility of the oxide NP in the matrix observed in many oxide–oxide systems favors the preparation of the homogeneous solid solutions with a high dopant content.

The preparation of composites containing magnetic nanoparticles in the amorphous or crystalline oxide Al_2O_3 matrix seems quite promising, since such materials manifest unusual and unique magnetic properties. For example, mesoporic silicon and titanium oxides doped with nanosize α-Fe_2O_3 particles are characterized by superparamagnetic properties [52, 53], although the α-Fe_2O_3 nanoparticles themselves are antiferromagnetic.

The magnetic properties of the double oxide Al_2O_3-Fe_2O_3 system are not studied completely enough. Most magnetic studies deal with an investigation of nanocomposite materials. For example, it is reported that the granulated thin Fe-Al_2O_3 films obtained by the implantation of Fe ions in α-Al_2O_3 single crystals demonstrate superparamagnetic behavior [54]; nanocomposite Fe-Al_2O_3 containing nanoparticles of the α-phase Fe with a Al_2O_3 shell (the sol-gel method [55]) are ferromagnetic. It was established that there is a transition from the ferromagnetic state at a low temperature into the superparamagnetic state at a temperature of 23 K for samples containing isolated quasispherical–spherical nanocrystals in the structured nanocomposite films consisting of the five Fe layers in the amorphous Al_2O_3 matrix (pulse laser deposition) [56], etc.

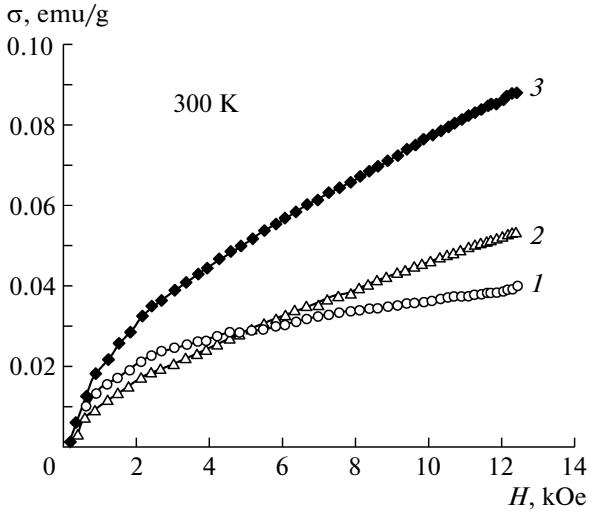

Fig. 6. Magnetization curves of NP Al_2O_3-Fe_2O_3 in the magnetic field of up to 12 kOe. (*1*) $x_{Fe} = 1.1\%$, (*2*) $x_{Fe} = 2.5$, and (*3*) $x_{Fe} = 4.2$.

The components of the Al_2O_3-Fe_2O_3 system in nanosize form demonstrate the ferromagnetic properties at room temperature. The magnetization of thin Al_2O_3 films (radio-frequency sputtering) [67] and NP Al_2O_3 (annealing $Al(OH)_3$ at 500°C) [68] reached 4.6 emu/cm^3 and 3.5×10^{-3} emu/g, respectively.

The second component of the system may be one form of iron(III) oxide-maghemite (γ-Fe_2O_3) or hematite (α-Fe_2O_3). Maghemite has strong ferromagnetic properties with the saturation magnetization of 80 emu/g. Hematite is a typical antiferromagnet with a Neel temperature of 680°C. However, at room temperature, the hematite particles (nanorods) behave like a weak ferromagnet with low saturation magnetization on the order of 0.6 emu/g [57] and sometimes demonstrate high saturation magnetization (~13 emu/g) [58]. The appearance of ferromagnetic properties in hematite [58] was associated with a large number of point defects in the sample, since after annealing the sample became antiferromagnetic. The irreversible phase transformation γ → α in NP Al_2O_3 prepared by the gas-phase method occurs at a temperature of 400°C. In nanocrystalline Fe_2O_3 prepared by wet chemistry, the transformation γ → α was fixed in the temperature range of 300–500°C depending on the experimental method used [59, 60]. The difference in the estimates of the temperature of the phase transition γ → α is not explained completely [61].

Therefore it was of certain interest to trace the evolution of the ferromagnetic response in NP Al_2O_3-Fe_2O_3 prepared by electron evaporation with an increase in the iron content in the diamagnetic Al_2O_3 matrix.

Magnetic measurements showed that all NP Al_2O_3-Fe_2O_3 prepared by electron evaporation had

weak ferromagnetic properties at room temperature (Fig. 6).

The maximum ferromagnetic response was established in the sample with the minimum Fe content = 1.1 wt % (Fig. 6, curve *1*). The magnetic moment per Fe atom in this sample was 3.8×10^{-2} μ_B/Fe. The calculated contribution from the Fe impurity in the zero valence state should have been much higher (2.2 emu/g), which indicates the absence of Fe in the free state in NP and is in agreement with the XRD data. The slope of the NP magnetization curves with an increasing concentration of Fe ions indicates an increase in the paramagnetic contribution that is quite reasonable taking into account that susceptibility should increase with an increasing iron concentration. The magnetic moment per Fe atom in the samples with the Fe content = 2.5 and 4.1 wt % was 2.2×10^{-2} and 1.9×10^{-2} μ_B/Fe, respectively.

Thus, the magnetic moment in the Al_2O_3-Fe_2O_3 system decreased with an increasing Fe concentration in the NP. The absence of information about the valence state of Fe ions in solid solutions of different iron phases in multiphase NP Al_2O_3-Fe_2O_3 did not make it possible to unambiguously conclude about the nature of ferromagnetism in these materials.

However, there is a large number of oxygen vacancies in NP (the increase in the mass of the NP (TG curve in Fig. 4a) due to the annealing of oxygen vacancies during heating above 500°C); the small amorphous fraction (Fig. 2a) and amorphous shells on the surface of separate NPs of the powder (Fig. 2b) (from Straumal et al. [62, 63] it is widely known that the ferromagnetic state may supported by a foamlike mesh on the boundaries of grains consisting of amorphous layers with different thicknesses) may lead to the appearance of magnetic moments localized on the oxygen vacancies. Therefore, most likely, ferromagnetism in NP Al_2O_3 and Al_2O_3-Fe_2O_3 is associated with the defect structure (oxygen vacancies) of powders. In addition, the maximum magnetic moment was recorded in the Al_2O_3-1.1% Fe sample with the minimum content of magnetic Fe ions, which is much less than the percolation threshold (usually several wt % of the dopant [64]). This fact confirms the opinion widespread among researchers of magnetism [45, 57, 58, 65, 66] about the absence of the logical correlation between the magnetic response and the concentration of the magnetic dopant in the diluted magnetic semiconductors. We note that the saturation magnetization in multiphase NP pure Al_2O_3 and Al_2O_3- Al in [16] (the content of Fe impurities in NP (ICP) did not exceed 6.07×10^{-2} and 3.9×10^{-2} wt %, respectively) reached (0.27–0.06)–(0.01–0.04) emu/g, respectively. We did not present the above data in [16] only because of the high magnetic inhomogeneity of the NP; however, the magnetic response of NP Al_2O_3 and Al_2O_3-Al, comparable in order of magnitude with the magnetization of NP Al_2O_3-Fe_2O_3 at a much lower content of magnetic Fe impurities (10^{-2} wt %) in undoped NP, directly indicates the important role of defects in the formation of magnetism in doped and undoped NPs on the basis of Al_2O_3.

Figure 7a shows the PCL spectra of multiphase NP [16] and A-NC coatings on the basis of pure Al_2O_3. Two broad bands in the green and red spectral regions were found in the spectrum of NP Al_2O_3. The spectrum of A-NC coatings of Al_2O_3 is characterized by a continuous wide band in the visible wavelength range of 350–900 nm. The clear difference in the PCL spectra of the powder and coatings of pure Al_2O_3, which were obtained under the same conditions (the difference is only in the evaporation time and the target-substrate distance), confirms their different phase compositions and the hypothesis about the dependence of the phase formation of coatings and NP upon the pulse electron evaporation on the deposition time of the NP.

Interestingly, the PCL spectra of coatings and NP of Al_2O_3-Fe_2O_3 (Figs. 7b, 7c) and the spectrum of A-NC coating of pure Al_2O_3 are similar (Fig. 7a). No dependence of the PCL spectra on the phase composition in the doped Fe_2O_3 powders and coatings was observed. Only a slight decrease in the cathode luminescence intensity with an increase in the Fe concentration was observed in both materials. A vivid peak at the wavelength of 695.09 nm on the PCL curve of the spectrum of NP with $x_{Fe} = 1.1\%$ (denoted by the symbol (*) in Fig. 7c) corresponds to α-Al_2O_3 and confirms the XRD data. The appearance of the peak of the α phase in the spectrum of NP Al_2O_3-Fe_2O_3 confirms the tendency of the preferential growth of the α phase in NPs at the low Fe doping level established in [17].

The studies of thermoluminescence (TL) and optically stimulated luminescence (OSL) in 12 samples of A-NC coatings and in 8 samples of NP of undoped Al_2O_3 prepared in one evaporation cycle showed that part of the samples of A-NC coatings has a considerable luminescence yield. Figure 8a shows typical TL curves of the samples of A-NC coatings (curves *1–3*); NP (curves *4–5*); and, for comparison, the TL curve of the sample of the TLD-500K dosimeter normalized to the mass of the coating (curve *6*). It follows from these data that the TL yield in all NP samples is two orders of magnitude less than that of the most emission-active samples of A-NC coatings and TLD-500K. In addition, it is of interest that annealing A-NC coatings at 350 (curve *1*), 400 (*2*), and 500°C (*3*) and NP at 350 (*4*) and 500°C (*5*) increases the luminescent activity, which is in good agreement with DSC-TG data about the initiation of the transitions "amorphous state $\rightarrow$ γ- phase" in the studied objects [69]. If the low TL and OSL responses of NPs and thin layers of Al_2O_3 were noted in many studies of their luminescent properties [70–72], their unusually high

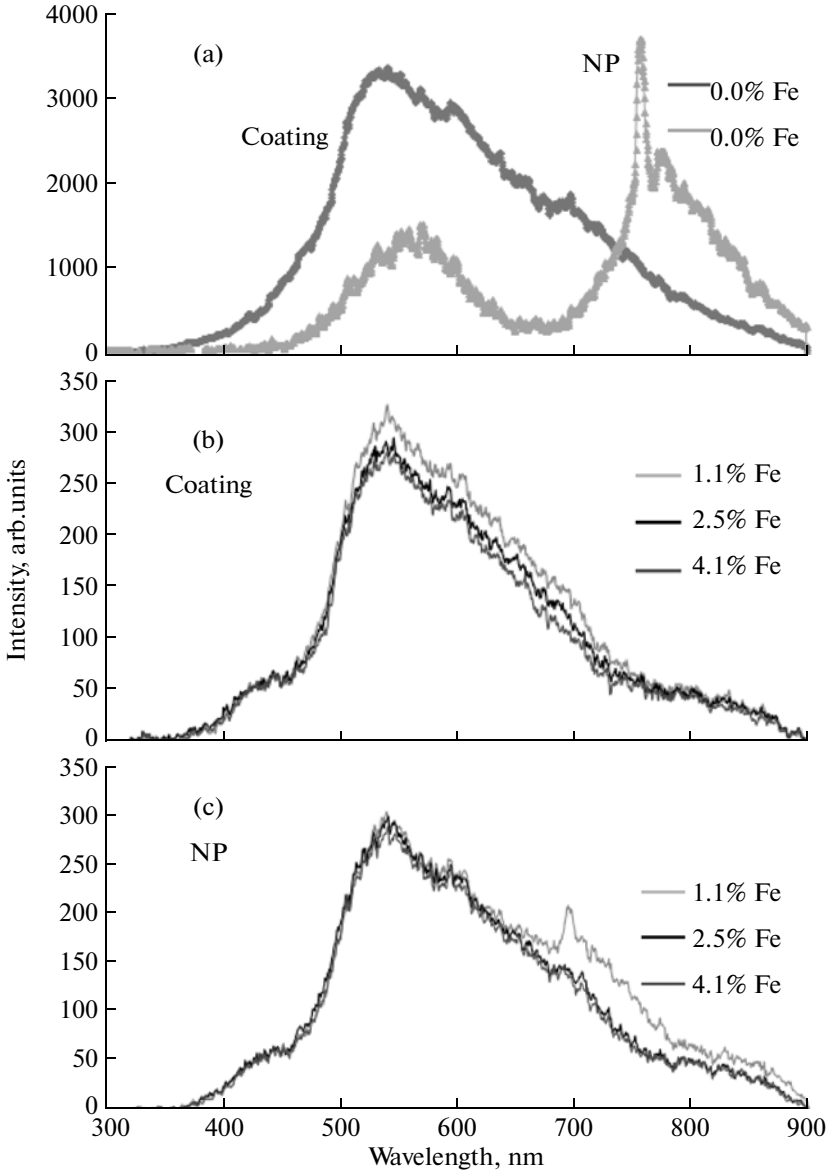

Fig. 7. PCL spectra: (a) NP and coatings of pure Al_2O_3, (b) coatings Al_2O_3-Fe_2O_3, and (c) NP Al_2O_3-Fe_2O_3.

values for part of the A-NC coatings synthesized in this work, which are comparable with the analogous ones for TLD-500K, were observed for the first time.

The introduction of the iron impurity in the samples of A-NC coatings considerably changes the TL curves and TL yield (Fig. 8b). The curves become more structurized; two maxima at 130 and 160°C and two features in the shape of shoulders at 80 and 200°C are observed on them. It is important to note that similar TL curves are observed in the α-Al_2O_3 crystals with transition metal impurities [73–76]. The TL yield decreases with a factor of 15 with increasing Fe impurity concentration from 1 to 5% and in comparison with undoped A-NC coatings with a factor of 50–75. Such a decrease in the TL response during the introduction of the low-activity Fe impurity is not anomalous. The doping of α-Al_2O_3 single crystals with transition metals, particularly in such high concentrations, may lead to the complete suppression of luminescent activity [74].

Nevertheless, the Al_2O_3-1% Fe_2O_3 samples have a TL yield of no less than that for NP layers and Al_2O_3 coatings prepared according to different technologies [70–72]. Moreover, since the phase transitions in the Al_2O_3-$(Fe_2O_3)_x$ system (x = 0–5%), as noted above, may take place both at low and at high temperatures, it is of interest to trace the transformation of the TL and OSL curves in the wide temperature range of annealing, by comparing, if possible, the similar dependence for A-NC coatings of Al_2O_3 and Al_2O_3-Fe_2O_3.

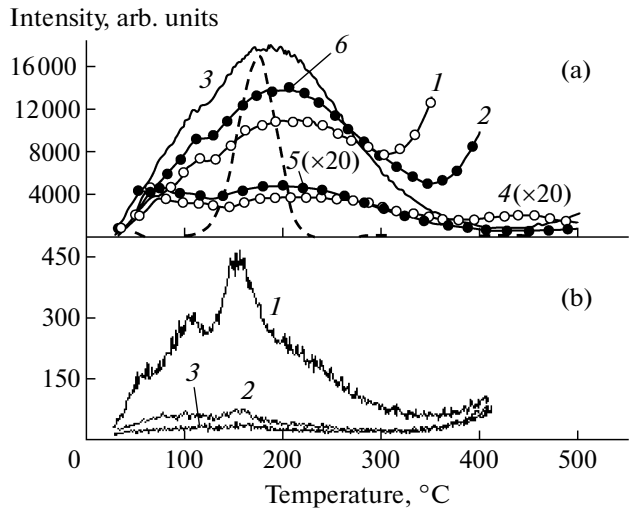

Fig. 8. (a) TL curves of the samples of the Al_2O_3 coating before (*1*–*3*) and NP Al_2O_3 (*4*, *5*) measured after annealing at 350°C (curves *1*, *4*), 400°C (*2*), 500°C (*3*, *5*), and the TLD-500K sample (*6*). (b) TL curves of the samples of the Al_2O_3-1% Fe_2O_3 coating (*1*), Al_2O_3-3% Fe_2O_3 (*2*), and Al_2O_3-5% Fe_2O_3 (*3*). The heating rate is 2°C/s; X-ray radiation dose is 3.6 Gy.

In this respect, first we selected two series of samples of A-NC coatings from the nominally pure Al_2O_3 with the minimum (type 1) and maximum (type 2) OSL and TL responses. The comparison of OSL and TL properties and the location of the substrate during PEB evaporation made it possible to establish that, under similar conditions (thickness of the coating and its homogeneity), the OSL and TL yields depended on the geometry of the location of the samples with respect to the plasma torch of the sputtered material.

In addition, it follows from the XRD data (Fig. 9) that in both types of samples the amorphous component dominates, which is manifested in diffractograms as a smooth curve of diffuse scattering, the same as in the sample of the type 1 with the small response (curve *a*). There are up to 10–20% of the γ phase in the samples of type 2 with the increased OSL and TL yield (curves *b*, *c*). Moreover, the diffractogram of the sample of type 2 (curve *d*) annealed at 300°C shows, in addition to the growth of the reflexes 311, 400, and 440 characteristic for the γ phase, reflex 222, which indicates the formation of new types of nasnocrystallites of the γ phase with the other orientation. The contribution of it was estimated from the intensity of characteristic reflexes 400 and 440 (card 00-029-0063 of the PDF-2 database) using the XRD Crystallinity program.

OSL decay curves typical for the samples of types 1 and 2 on the glass substrate are shown in Fig. 10a at the X-ray irradiation dose $D_X = 3.6$ Gy. It is seen that they differ by the OSL response (curves *1*, *2*) with a factor of no less than two. Moreover, the OSL yields normalized for the mass of the sensitive layer are comparable for the sample of type 2 and the TLD-500K detector with average sensitivity (curves *2* and *3*).

An analysis of the data makes it possible to suppose that the luminescent properties of the studied nanostructured Al_2O_3 layers are related to the content of the γ phase in them. If one takes into account that the transition in the γ phase occurs at T = 130–650°C [77], one should expect, like in the case with TL, a considerable increase in the OSL yield with an increasing annealing temperature of the samples. Figure 10b and its inset show separate OSL decay curves for the type-2 sample and the general change in the integral yield S_{OSL} (light sum) depending on the tem-

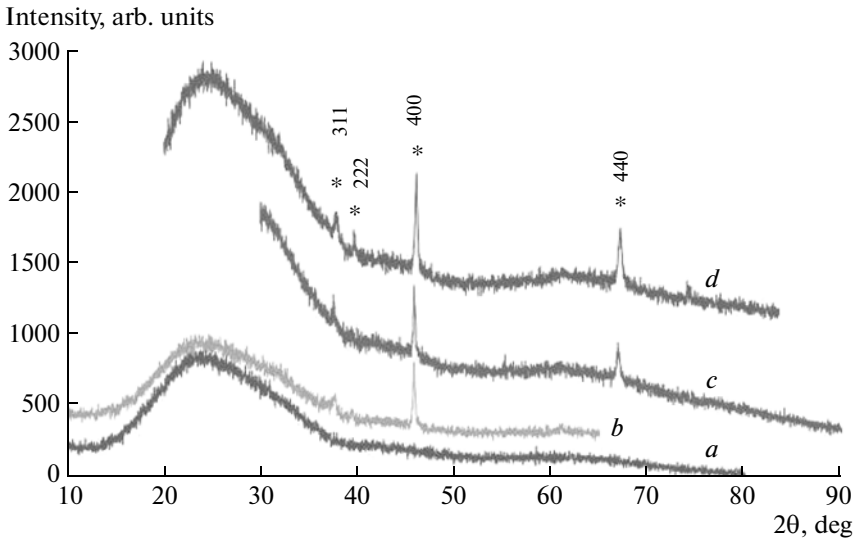

Fig. 9. (*a*) Diffractogram of the amorphous coating, (*b*, *c*) diffractograms of the A-NC coating before annealing in angles θ = 10–65° and θ = 30–90°, and (*d*) diffractogram of the A-NC coating after annealing. *Miller indices for the γ-phase Al_2O_3.

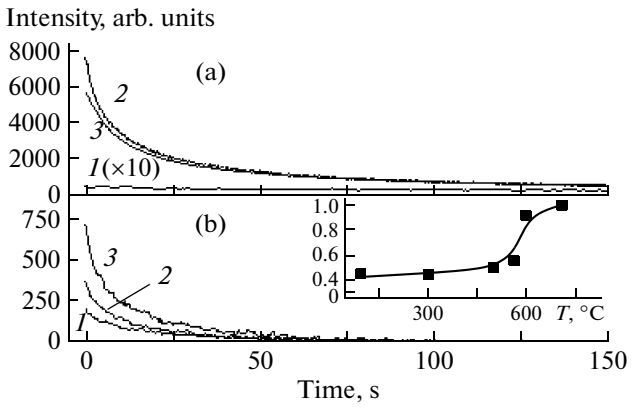

Fig. 10. (a) OSL decay curves of the samples of type 1 (*1*) and 2 (*2*), TLD-500K detector (*3*) at T = 25°C and D_X = 3.6 Gy. (b) OSL curves of the sample of type 2 measured at T = 25°C, D_X = 0.1 Gy after isochronous annealing at T_{A1} = 300°C (*1*), T_{A2} = 550°C (*2*), and T_{A3} = 700°C (*3*) and the dependence $S_{OSL}(T_A)$ (inset).

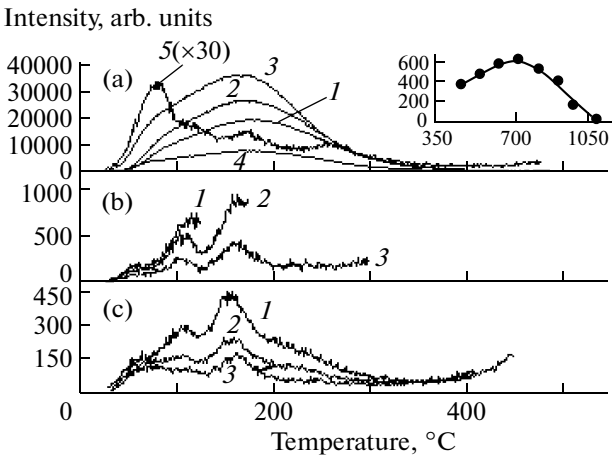

Fig. 11. TL curves of the samples of (a) coatings Al_2O_3 and (b, c) Al_2O_3-1% Fe_2O_3 measured at isochronous annealing up to 1150°C. Inset shows the dependence $S_{TL}(T_A)$ for the coating Al_2O_3. The heating rate is 2°C/s; X-ray radiation dose is D_X = 3.6 Gy.

perature of the isochronuos annealing T_A up to 700°C for 10 min in air. It is seen that our assumption is confirmed: after a more complete transition of the studied nanostructured Al_2O_3 layers into the γ phase, the OSL yield increases with a factor of no less than 2–2.5. The subsequent temperature increase (T_A > 700°C) led to the breakaway of the coating from the substrate of quartz glass. Nevertheless, annealing at increased temperatures is of interest, since it will favor the transition of the γ phase in more ordered and densely packed crystal shapes: δ(970°C) → θ(1050°C) → α(1150°C) [77]; the anion-defective modification α-Al_2O_3 has one of the highest TL and OSL yields [78].

Further studies were directed at studying TL properties of the type-2 samples annealed up to 1150°C. Steel was chosen for substrates as a good thermally conductive and more refractory material than quartz glass. In addition, the steel substrate in regards to its summary physicochemical properties (melting temperature, adhesion characteristics, linear coefficient of thermal expansion) fits experiments on annealing up to 1150°C better.

Figure 11a shows the separate TL curves of the sample of the coating of undoped Al_2O_3 on the steel substrate (curves *1*–*5*) and the change of the integral TL yield S_{TL} (inset) depending on the temperature of the isochronous annealing in the range of 500–1150°C. Like in the case of analogous dependences in the study of OSL (Fig. 10b), the TL yield increases with a factor of ~2 with an increase in annealing temperature up to 700°C (annealing at 400°C is shown by curve *1*, at 500°C by curve *2*, and at 700°C by curve *3*). A further increase in temperature to 1150°C (curve *4*) leads to a considerable decrease in the TL yield. The TL curve after annealing at 1150°C changes strongly: three low-intensity narrow peaks are observed on it at 80, 160, and 270°C. Here it is necessary to underline the partial coincidence of the given extrema on the TL curve after annealing at 1150°C with analogous ones for the sample of the coating Al_2O_3-1% Fe_2O_3 (Fig. 8b, curve *1*). One of the main origins of the observed decrease in the TL yield of A-NC coatings of Al_2O_3 and the dramatic transformation of the TL curve after annealing at 1150°C may be the recovery of the stoichiometric composition in the annealed Al_2O_3 sample as indicated by the DSC-TG and gas-isolation data (Figs. 4, 5).

The change in the TL curves of the sample of the coating Al_2O_3-1% Fe_2O_3 at isochronous annealing up to 1150°C was studied for an additional confirmation of the obtained regularities about the connection of the luminescent yield with the phase transitions in the nanostructured aluminum oxide. Taking into account the possible decrease in the temperature thresholds of such transitions in the Al_2O_3-Fe_2O_3 system (as was noted above), the detailed measurements of the transformation of the TL curves were performed with a smaller step in the process of the isochronous annealing up to 350°C. It is seen (Fig. 11b) that the intensity of the TL maximum at 110°C is reached after annealing at 125°C (curve *1*); the maximum at 160°C is at 175°C (curve *2*). A further increase in the temperature to 300°C (curve *3*) decreases the intensity of these maxima with a factor of ~2. The growth in annealing temperature to 500–700°C almost does not change the TL curves. The second stage of the considerable decrease (with a factor of 3) in the TL yield is observed in the range of 700–1150°C (Fig. 11c). As a result of annealing at 1150°C, the TL curve (curve *3*) is transformed to a shape close to the TL curve of the

annealed sample of the A-NC coating Al_2O_3 with the analogous maxima (Fig. 11a, curve *5*).

Consequently, the data may indicate a decrease in the temperature threshold in the nanostructured Al_2O_3-Fe_2O_3 system during the amorphous-state–crystal phase transition. Moreover, it is possible to propose an assumption on the basis of the combined analysis of XRD, DSC-TG data, the isolation rate of H_2O and CO_2, and the transformation of the TL curves at isochronous annealing and taking into account their comparison with similar data for undoped samples of coatings. This assumption requires further confirmations. It includes the fact that, with increasing temperature, the phase transitions in coatings with the Al_2O_3-(1–5)% Fe_2O_3 composition occur, with high probability, from the amorphous state into more perfect crystal forms (δ, θ, α) without the formation of new Al_2O_3 nanocrystals of the luminescence-active γ-form.

Thus, summing up the studies of the luminescent properties of the nanostructured coatings and NPs Al_2O_3 prepared by pulsed electron evaporation, it is necessary to note, that under some conditions, it is possible to create a thin-layer material promising for accumulation luminescent β-dosimetry. It was shown experimentally that part of the nanostructured coatings of nominally pure Al_2O_3 has increased OSL and TL yields comparable with similar ones for one of the leaders among TL and OSL detectors (TLD-500K) [78]. It was also established that the high luminescent yield of the coatings correlates with the content of the γ phase of Al_2O_3 in them.

CONCLUSIONS

Coatings and multiphase NPs on the basis of pure and iron-doped Al_2O_3 are prepared by pulsed electron evaporation in vacuum. The specific surface of NP Al_2O_3-Fe_2O_3 reached 277 m^2/g. The deposition duration of NP affected the phase composition of coatings and NP. The α- and θ-phase Al_2O_3 were found in a composition of NP that is not typical for gas-phase methods. The crystalline γ phase was formed in A-NC coatings. The phase transformations in NP Al_2O_3 and the coating of Al_2O_3-Fe_2O_3 (1.1% Fe) took place according to the amorphous phase $\rightarrow \gamma \rightarrow \delta \rightarrow \theta \rightarrow \alpha$ scheme. Iron doping decreases the temperature of the threshold of the crystallization of the amorphous phase in coatings of Al_2O_3-Fe_2O_3 and thermally and optically suppresses the stimulated luminescence of coatings with increasing iron concentration. Cathode luminescent spectra of Fe-doped coatings slightly differ from the spectra of NP Al_2O_3-Fe_2O_3 regardless of the dopant concentration (1–4 wt % Fe), which indicates the same mechanism of luminescence of the materials regardless of their phase composition. On the contrary, the effect of the phase composition on the PCL spectra is traced in NP and coatings of pure and Cu- and Al-doped Al_2O_3. The crystallization of the amorphous component in NP and coatings of undoped Al_2O_3 is terminated at a temperature of about 830°C. All NP Al_2O_3–Fe_2O_3 showed ferromagnetic behavior at room temperature.

These results indicate the elaboration of promising nanotechnology for the preparation of a new thin-layer detector material on the basis of nanostructured Al_2O_3 that highly effectively stores the energy of the ionizing radiations and is luminescent at optical and thermal stimulation and also applicable for the dosimetry of the β-radiation and soft component (≤30 keV) of the photon radiation.

The magnetic-luminescent properties and the small size of the particles (3–40 nm) of NP and coatings on the basis of Al_2O_3 make them promising for further use in spintronics, biomedicine (lumineschent markers), medicine (contrast means for the ultrasonic visualization), and ceramic synthesis (active nanoadditives) and as catalysts, gas and humidity sensors, and other applications.

ACKNOWLEDGMENTS

We are grateful to M.A. Uimin (Institute of Metal Physics, Ural Branch, Russian Academy of Sciences) for our discussions and for measuring the magnetic characteristics, S.V. Pryanichnikov (TsKP URAL, Institute of Metallurgy, Ural Branch, Russian Academy of Sciences) for the XRD analysis, T.M. Demina (Institute of Electrophysics, Ural Branch, Russian Academy of Sciences) for an analysis of the specific surface and measurement of the DSC-TG curves, A.M. Murzakaev (Institute of Electrophysics, Ural Branch, Russian Academy of Sciences) for the microscopic analysis, and A.V. Spirina (Institute of Electrophysics, Ural Branch, Russian Academy of Sciences) for the measurement of the cathode luminescence spectra. This work was supported in part by the Presidium of the Ural Branch of the Russian Academy of Sciences (grant no. 12-U-2-032).

REFERENCES

1. W. Engelhart, W. Dreher, O. Eibl, and V. Schier, "Deposition of alumina thin film by dual magnetron sputtering: Is it γ-Al_2O_3?," Acta Mater. **59**, 7757–7767 (2011).
2. O. Zywitzki, G. Hoetzsch, F. Fietzke, and K. Goedicke, Effect of the substrate temperature on the structure and properties of Al_2O_3 layers reactively deposited by pulsed magnetron sputtering," Surf. Coat. Technol. **82**, (1–2), 169–175 (1996).
3. O. Kyrylov, D. Kurapov, and J. M. Schneider, "Effect of ion irradiation during deposition on the structure of alumina thin films grown by plasma assisted chemical vapour deposition," Appl. Phys. A: Mater. Sci. Processing **80** (8), 1657–1660 (2005).

4. J. M. Andersson, Zs. Czigány, P. Jin, and U. Helmersson, "Microstructure of α-alumina thin films deposited at low temperatures on chromia template layers," J. Vac. Sci. Technol. A **22**, 117–121 (2004).
5. P. Jin, G. Xu, M. Tazawa, K. Yoshimura, D. Music, J. Alami, and U. Helmersson, "Low temperature deposition of α-Al_2O_3 thin films by sputtering using a Cr_2O_3 template," J. Vac. Sci. Technol. A. **20**, 2134–2136 (2002).
6. J. M. Andersson, E. Wallin, U. Helmersson, U. Kreissig, and E. P. Munger, "Al_2O_3 thin films grown at low temperatures," Thin Solid Films **513**, 57–59 (2006).
7. P. Eklund, M. Sridharan, G. Singh, and J. Bottiger, "Thermal Stability and Phase Transformations of γ-/Amorphous-Al_2O_3," Thin Films Plasma Processes Polym.s **6** (S1), S907–S911 (2009).
8. X. F. Duan, N. H. Tran, N. K. Roberts, and R. N. Lamb, "Solvothermal approach for low temperature deposition of aluminium oxide thin films," Thin Solid Films **518** (15), 4290–4293 (2010).
9. V. Edlmayr, M. Moser, C. Walter, and C. Mitterer, "Thermal stability of sputtered Al_2O_3 coatings," Surf. Coat. Technol. **204**, 1576–1581 (2010).
10. T. Kohara, H. Tamagaki, Y. Ikari, and H. Fujii, "Deposition of a-Al_2O_3 hard coatings by reactive magnetron sputtering," Surf. Coat. Technol. **185**, 166–171 (2004).
11. R. Romàn, T. Hernàndez, and M. Gonzàlez, "Nano or micro grained alumina powder? A choose before sintering," Boletín de la Sociedad Española de Cerámica y Vidrio **47** (6), 311–318 (2008).
12. G. R. Karagedov and A. L. Myz, "Preparation and sintering pure nanocrystalline α-alumina powder," J. Europ. Ceram. Soc. **32** (1), 219–225 (2012).
13. K. Yatsui, T. Yukawa, C. Grigoriu, M. Hirai, and W. Jiang, "Synthesis of ultrafne γ-Al_2O_3 powders by pulsed laser ablation," J. Nanopart. Res. **2** (1), 75–83 (2000).
14. D. A. Dubov, Vl. Snytnikov, and V. N. Snytnikov, "The way to synthesize nanopowders of churlish oxides by means of laser evaporation," in *Collection of Scientific Papers of Novosibirsk State Technical University* (Novosibirsk, 2005), No. 4(42), pp. 83–90 [in Russian].
15. S. P. Bardakhanov, A. I. Korchagin, N. K. Kuksanov, A. V. Lavrukhin, R. A. Salimov, S. N. Fadeev, and V. V. Cherepkov, "Use of an electron accelerator to produce nanopowders by evaporation of initial materials at atmospheric pressure," Russ. Phys. J. **50** (2), 120–124 (2007).
16. V. G. Il'ves, A. I. Medvedev, A. M. Murzakaev, S. Yu. Sokovnin, A. V. Spirina, and M. A. Uimin, "Physiscal characteristics of Al_2O_3-Al(Cu) nanopowders synthesized by target electron-beam evaporation," Fiz. Khim. Obrab. Mater., No. 2, 65–70 (2011).
17. S. Schlabach, V. Szabó, D. Vollath, A. Braun, and R. Clasen, "Structure of alumina and zirconia nanoparticles synthesized by the Karlsruhe Microwave Plasma Process," Solid State Phenom. **99–100**, 191–196 (2004).
18. K. Jiang, K. Sarakinos, S. Konstantinidis, and J. M. Schneider, "Low temperature synthesis of α-Al_2O_3 films by high-power plasma-assisted chemical vapor deposition," J. Phys. D: Appl. Phys. **43**, 325202 (15) (2010).
19. D. L. Alontseva, S. N. Bratushka, A. D. Pogrebnyak, N. V. Prokhorenkova, and V. T. Shablya, "Structure and properties of coatings and modified layers synthesized by means of plasma flows," Fiz. Inzh. Poverkhn. **5** (3–4), 124–139 (2007).
20. A. D. Pogrebnyak, M. I. Il'yashenko, S. N. Bratushka, V. V. Ponaryadov, and N. K. Erdybaeva, "The way for forming high-dispersed state in plasma-detonating aluminum oxide coating," Fiz. Inzh. Poverkhn. **4** (1–2), 32–47 (2006).
21. I. Levin and D. Brandon, "Metastable Alumina Polymorphs: Crystal Structures and Transition Sequences," J. Am. Ceram. Soc. **81** (8), 1995–2012 (1998).
22. L. A. Krushinskaya and Ya. A. Stel'makh, "Structure and properties of aluminum oxide thick condensates synthesized by electron-beam evaporation and deposition of vapor phase in vacuum," VANT. Ser.: Chist. Mater. Vakuum. Tekhnol. **19** (6), 92–98 (2011).
23. E. Krumov, V. Mankov, and K. Starbova, "Nanosized columnar microstructure and related properties of electron gun deposited Al_2O_3 thin films," Vacuum **76**, 211–214 (2004).
24. H. H. Huang, Y. S. Liu, Y. M. Chen, M. C. Huang, and M. C. Wang, "Effect of oxygen pressure on the microstructure and properties of the Al_2O_3-SiO_2 thin films deposited by E-beam evaporation," Surf. Coat. Technol. **200**, 3309–3313 (2006).
25. N. Yu, T. W. Simpson, P. C. McIntyre, M. Nastasi, and I. V. Mitchell, "Doping effects on the kinetics of solid phase epitaxial growth of amorphous alumina thin films on sapphire," Appl. Phys. Lett. **67**, 924–926 (1995).
26. V. S. Kortov, I. I. Mil'man, and S. V. Nikiforov, "Solid dosimetry," Izv. Tomsk. Politekhn. Univ. **303** (2), 35–45 (2000).
27. C. E. Chryssou and C. W. Pitt, "Al_2O_3 thin films by plasma-enhanced chemical vapor deposition using trimethyl-amine alane (TMAA) as the Al precursor," Appl. Phys. A **65**, 469–475 (1997).
28. Yu. A. Kotov, S. Yu. Sokovnin, V. G. Il'ves, and C. K. Rhee, RF Patent 2353573 B82B 3/00, Byull. Izobret., No. 12 (2009).
29. S. G. Mikhailov, V. V. Osipov, and V. I. Solomonov, "Pulse cathodoluminescent KLAVI 1 AU device for matter analyzing," Prib. Tekhn. Eksperim., No. 3, 164–165 (2001).
30. I. I. Mil'man, E. V. Moiseikin, S. V. Nikiforov, S. V. Solov'ev, I. G. Revkov, and E. N. Litovchenko, "Role of deep traps in luminescence of α-Al_2O_3:C anion-defect crystals," Fiz. Tverd. Tela **50** (11), 1991–1995 (2008).
31. A. K. Ladavos and T. V. Bakas, "The Al_2O_3-Fe_2O_3 mixed oxidic system, I. Preparation and characterization," React. Kinet. Catal. Lett. **73** (2), 223–228 (2001).
32. S. Yu. Sokovnin, V. G. Il'ves, and S. V. Pryanichnikov, "Structure and magnetic properties of ZnO nanopowders doped by ferrum," Zh. Tekh. Fiz. (2013) (in press).
33. C. Oprea and V. Ionescu, "TEM and XRD investigation of Fe_2O_3-Al_2O_3 system," Ovidius Univ. Ann. Chem. **20** (2), 222–226 (2009).

34. A. D. Pogrebnyak, Yu. N. Tyurin, Yu. F. Ivanov, A. P. Kobzev, O. P. Kul'ment'eva, and M. V. Il'yashenko, "The way to produce and investigate structure and properties of Al_2O_3 plasma-detonating coatings," Pis'ma Zh. Tekh. Fiz. **26** (21), 3–60 (2000).

35. R. Nakamura, T. Shudo, A. Hirata, M. Ishimaruand, and H. Nakajima, "Nanovoid formation through the annealing of amorphous Al_2O_3 and WO_3 films," Scripta Mater. **64**, 197–200 (2011).

36. R. Nakamura, M. Ishimaru, A. Hirata, K. Sato, M. Tane, H. Kimizuka, T. Shudo, T. J. Konno and H. Nakajima, "Enhancement of nanovoid formation in annealed amorphous Al_2O_3 including W," J. Appl. Phys. **110**, 064324 (7) (2011).

37. E. Yu. Svetkina, "Mechanical-chemical variations of Al_2O_3 under vibration," Vopr. Khim. Khim. Tekhnol., No. 4, 36–41 (2003).

38. R. S. Gates, S. M. Hsu, and E. E. Klaus, "Tribochemical mechanism of alumina with water," Tribol. Trans **32** (3), 357–363 (1989).

39. E. S. Astapova, E. B. Pivchenko, and E. A. Vanina, "Transition α γ for aluminum oxide in corundum ceramic caused by neutron radiation," Dokl. Akad. Nauk **376** (5), 611–614 (2001).

40. Z. Zhou, H. Guo, M. Abbas, and S. Gong, "Effect of water vapor on the phase transformation of alumina grown on NiAl at 950C," Corrosion Sci. **53**, 2943–2947 (2011).

41. F. Pan, C. Song, X. J. Liu, Y. C. Yang, and F. Zeng, "Ferromagnetism and possible application in spintronics of transition-metal doped ZnO films," Mater. Sci. Eng. **62**, 1–35 (2008).

42. T. Dietl, "A ten-year perspective on dilute magnetic semiconductors and oxides," Nature Mater. **9**, 965–974 (2010).

43. J. M. D. Coye and S. Chambers, "Oxide dilute magnetic semiconductors-fact or fiction?," MRS Bull. **33**, 1053–1058 (2008).

44. J. M. D. Coey, "d0 Ferromagnetism," Solid State Sci. **7**, 660–667 (2005).

45. A. Sundaresan, R. Bhargavi, N. Rangarajan, U. Siddesh, and C. N. R. Rao, "Ferromagnetism as a universal feature of nanoparticles of the otherwise nonmagnetic oxides," Phys. Rev. B **74** (16), 161304 (4) (2006).

46. Y. L. Zheng, C. M. Zhen, X. Q. Wang, L. Ma, X. L. Li, and D. L. Hou, "Room-temperature ferromagnetism observed in alumina films," Solid State Sci. **13** (8), 1516–1519 (2011).

47. V. G. Il'ves and S. Yu. Sokovnin, "The way to synthesize ZnO and Zn-ZnO nanopowders by means of pulse electron beam evaporation in low pressure gas," Ross. Nanotekhnol. **6** (1–2), 20–26 (2011).

48. S. Yu. Sokovnin, V. G. Il'ves, A. I. Medvedev, A. M. Murzakaev, and M. A. Uimin, "Pulse electron evaporation of ZnO-Zn nanopowders doped by cuprum," in *Proc. 4th All-Russian Conf. on Nanomaterials* (A. Baikov Institute of Metallurgy and Materials Science, Moscow, March 1–4, 2011), pp. 128, 574.

49. S. Yu. Sokovnin and V. G. Il'ves, *The Way to Use Pulse Electron Beam for Synthesizing Metal Oxide Powders* (Ural Brunch RAS, Yekaterinburg, 2011) [in Russian].

50. V. G. Il'ves and S.Yu. Sokovnin, "The way to produce and investigate properties of CeO_2 nanopowders," Ross. Nanotekhnol. **7** (3–4), 7–16 (2012).

51. V. G. Il'ves and S. Yu. Sokovnin, "Magnetic properties of ZnS nanopowders synthesized by means of pulse electron beam," in *Interuniversity Collection of Papers "Problems of Spectroscopy and Spectrometry* (Ural State Tech. Univ., Yekaterinburg, 2010), Issue 26, pp. 237–242 [in Russian].

52. T. K. Kundu, M. Mukherjee, and D. Chakravorty, "Growth of nano-α-Fe_2O_3 in a titania matrix by the sol-gel route," J. Mater. Sci. **33**, 1759–1763 (1998).

53. M. Tadic, D. Markovic, V. Spasojevic, V. Kusigerski, M. Remskar, J. Pirnat, and Z. Jaglicic, "Synthesis and magnetic properties of concentrated α-Fe_2O_3 nanoparticles in a silica matric," J. Alloys Compounds **441** (1–2), 291–296 (2007).

54. I. Sakamoto, S. Honda, H. Tanoue, N. Hayashi, and H. Yamane, "Structural and magnetic properties of Fe ion implanted Al_2O_3," Nucl. Instrum. Methods Phys. Res. Sect. B: Beam Interact. Mater. Atoms **148** (1–4), 1039–1043 (1999).

55. D. S. Xue, Y. L. MaY. Huang, P. H. Zhou, Z. P. Niu, F. S. Li, R. Job, and W. R. Fahrner, "Magnetic properties of pure Fe-Al_2O_3 nanocomposites," J. Mater. Sci. Lett. **22**, 1817–1820 (2003).

56. N. M. Dempsey, L. Ranno, D. Givord, J. Gonzalo, R. Serna, G. T. Fei, A. K. Petford-Long, R. C. Doole, and D. E. Hole, "Magnetic behavior of Fe:Al_2O_3 nanocomposite films produced by pulsed laser deposition," J. Appl. Phys. **90** (12), 6268–6274 (2001).

57. R. Ramesh, K. Ashok, G. M. Bhalero, S. Ponnusamy, and C. Muthamizhchelvan, "Synthesis and properties of α-Fe_2O_3 nanorods, "Cryst. Res. Technol. **45** (9), 965–968 (2010).

58. J. Wu, S. Mao, Z. G. Ye, Z. Xie, and L. Zheng, "Room-temperature weak ferromagnetism induced by point defects in alpha-Fe_2O_3," Appl. Mater. Interfaces **2** (6), 1561–1564 (2010).

59. G. Schimanke and M. Martin, "In situ XRD study of the phase transition of nanocrystalline maghemite (γ-Fe_2O_3) to hematite (α-Fe_2O_3)," Solid State Ionics **136–137**, 1235–1240 (2000).

60. G. Ennas, G. Marongiu, A. Musinu, A. Falqui, P. Ballirano, and R. Caminiti, "Characterization of Nanocrystalline g-Fe_2O_3 Prepared by Wet Chemical Method," J. Mater. Res. **14**, 1570–1575 (1999).

61. O. Kido, Y. Higashino, K. Kamitsuji, M. Kurumada, T. Sato, Y. Kimura, H. Suzuki, Y. Saito, and C. Kaito, "Phase Transition Temperature of γ-Fe_2O_3 Ultrafine Particle," J. Phys. Soc. Jpn. **73**, 2014–2016 (2004).

62. B. B. Straumal, A. A. Myatiev, P. B. Straumal, A. A. Mazilkin, S. G. Protasova, E. Gering, and B. Baretzky, "Grain boundary layers in nanocrystalline ferromagnetic zinc oxide," Pis'ma Zh. Eksp. Teor. Fiz. **92** (6), 438–443 (2010).

63. B. B. Straumal, A. A. Mazilkin, S. G. Protasova, A. A. Myatiev, P. B. Straumal, G. Schütz, P. A. van Aken, E. Goering, and B. Baretzky, "Magnetization study of nanograined pure and Mn-doped ZnO films: Formation of a ferromagnetic grain-boundary foam," Phys. Rev. B **79**, 205206(6) (2009).

64. K. Sato and L. Bergqvist, J. Kudrnovský, P. H. Dederichs, O. Eriksson, I. Turek, B. Sanyal, G. Bouzerar, H. Katayama-Yoshida, V. A. Dinh, T. Fukushima, H. Kizaki, and R. Zeller, "First-principles theory of dilute magnetic semiconductors," Rev. Mod. Phys. **82** (2), 1633–1690 (2010).

65. L. I. Burova, N. S. Perov, A. S. Semisalova, V. A. Kulbachinskii, V. G. Kytin, V. V. Roddatis, A. L. Vasiliev, and A. R. Kaul, "Effect of the nanostructure on room temperature ferromagnetism and resistivity of undoped ZnO thin films grown by chemical vapor deposition," Thin Solid Films **520**, 4580–4585 (2012).

66. D. Gao, Z. Zhang, J. Fu, Y. Xu, J. Qi, and D. Xue, "Room temperature ferromagnetism of pure ZnO nanoparticles," J. Appl. Phys. **105** (4), 113928(4) (2009).

67. Y. L. Zheng, C. M. Zhen, X. Q. Wang, X. L. Li, and D. L. Hou, "Room-temperature ferromagnetismobserved in alumina films," Solid State Sci. **13** (8), 1516–1519 (2011).

68. A. Sundaresan, R. Bhargavi, N. Rangarajan, U. Siddesh, and C. N. R. Rao, "Ferromagnetism as a universal feature of nanoparticles of the otherwise nonmagnetic oxides," Phys. Rev. B, Condens. Matter Mater. Phys. **74** (16), 161306(6) (2006).

69. S. Yu. Sokovnin and V. G. Il'ves, "Properties of nanopowders and coatings base on aluminum oxide synthesized by electron beam evaporation," Ross. Nanotekhnol. (2013) (in press).

70. M. W. Blair, L. G. Jacobsohn, S. C. Tornga, O. Ugurlu, B. L. Bennett, E. G. Yukihara, and R. E. Muenchausen, "Nanophosphor aluminum oxide: Luminescence response of a potential dosimetric material," J. Luminescence **130**, 825–831 (2010).

71. P. Mancosu, M. C. Cantone, I. Veronese, and A. Giussani, "Spatial distribution of beta extremity doses in nuclear medicine: a feasibility study with thin α-Al_2O_3:C TLDs," Phys. Med. **26**, 44–48 (2010).

72. J. E. Villarreal-Barajas, L. Escobar-Alarcón, E. Camps, P. R. Gonzales, and E. Villagran, "Thermoluminescence response of aluminum oxide thin films to beta-particle and UV radiation," Superficies y Vacío **13**, 126–129 (2001).

73. G. P. Summers, "Thermoluminescence in single crystal α-Al_2O_3," Radiat. Prot. Dosim. **8** (1–2), 69–80 (1984).

74. T. S. Bessonova, M. P. Stanislavskii, A. I. Sobko, and V. Ya. Khaimov-Mal'kov, "Concentration relationship of radiation-optical effects in ruby," J. Prikl. Spektroskop. **27** (2), 238–243.

75. A. I. Surdo, V. S. Kortov, and F. F. Sharafutdinov, "Luminescence of anion-defective corundum with titanium impurity," Radiat. Prot. Dosim. **84**, 261–264 (1999).

76. Ya. A. Valbis, P. A. Kulis, L. N. Raiskaya, V. A. Sandulenko, M. E. Springis, and Z. Z. Eromanov, "Recombination luminescence of α-Al_2O_3 crystals with admixture of IV group elements," in *Collection of Scientific Works of Latvian State University "Thermoactivating Spectroscopy for Defects in Ion Crystals"* (Riga, 1983), pp. 126–144 [in Russian].

77. R. S. Zhou and R. L. Snyder, "Structures and transformation mechanisms of the η, and γ transition aluminas," Acta Cryst. **47**, 617–630 (1991).

78. E. G. Yukihara and S. W. S. McKeever, *Optically Stimulated Luminescence: Fundamentals and Applications* (Jonn Wiley and Sons, Chichester, 2011).

Translated by L. Mosina